A Metal‑Semiconductor Platform with Enhanced Volatile‑Compound Sensing Performance

Authors: Zelio Fusco[1], Mohsen Rahmani[2], Thanh Tran-Phu[1], Chiara Ricci[1], Alexander Kiy[3], Patrick Kluth[3], Enrico Della Gaspera[4], Nunzio Motta[5], Dragomir Neshev[6] and Antonio Tricoli[1*]

Affiliations:

[1] Nanotechnology Research Laboratory, College of Engineering and Computer Science, The Australian National University, ACT 2601, Australia

[2] Advanced Optics and Photonics Laboratory, Department of Engineering, School of Science and Technology, Nottingham Trent University, Nottingham, NG11 8NS, UK

[3] Electronic Materials Engineering, Research School of Physics and Engineering, The Australian National University, ACT 2601, Australia

[4] Applied Chemistry and Environmental Science, RMIT, Melbourne, Vic 3001, Australia

[5] Institute for Future Environments and School of Chemistry, Physics, and Mechanical Engineering, Queensland University of Technology, Brisbane, QLD 4001, Australia

[6] ARC Centre of Excellence for Transformative Meta-Optical Systems, Research School of Physics, Australian National University, Canberra ACT, 2601, Australia

*Correspondence to: antonio.tricoli@anu.edu.au

Abstract: Advance of photonics media is restrained by the lack of structuring techniques for the three-dimensional fabrication of active materials with long-range periodicity. We report a methodology for the engineering of tunable resonant photonic media with thickness exceeding the plasmonic near-field enhancement region by more than two orders of magnitude. Our media architecture consists of a stochastically ordered distribution of plasmonic nanocrystals in a fractal scaffold of high-index semiconductors. This plasmonic-semiconductor fractal media supports the propagation of surface plasmons with drastically enhanced intensity over multiple length scales, overcoming two-dimensional limitations of established metasurface technologies. We use our fractal media for the fabrication of plasmonic optical gas sensors, achieving a limit of detection of 0.01 vol% at room temperature and sensitivity up to 1.9 nm/vol%, demonstrating almost a fivefold increase with respect to an optimized planar geometry. Beneficially to their implementation, the self-assembly mechanism of this fractal architecture allows fabrication of micrometer-thick media over surfaces of several square centimeters in a few seconds. The designable optical features and intrinsic scalability of these photonic fractal metamaterials provide ample opportunities for applications, bridging across transformation optics, sensing and light harvesting.

Keywords: fractal, sensors, plasmonic, multiscale, three-dimensional metamaterials

Introduction

Progress in the understanding of nanoscale light-matter interaction has led to the realization of photonics metamaterials, displaying uncommon characteristics such as negative refraction, cloaking, optical chirality, hyperbolicity and epsilon-near-zero properties[1]. Materials with sub-diffraction resonant behaviors, such as localized surface plasmon resonance (LSPR), can now be designed across the entire visible and near infrared region of the electromagnetic spectrum by engineering the collective oscillation of free electrons in nanostructures[2]. This unprecedented control over the spatial and temporal propagation of electromagnetic waves is paving the way to a plethora of applications. The latter include structural color displays[3], electromagnetic energy harvesting[4] and transport[5], photocatalysis[6], quantum plasmonics[7] as well as miniaturized bio- and chemical molecule sensing[8, 9].

Structuring of three-dimensional photonic media is required to overcome some intrinsic limitations of current technologies that are largely based on two dimensional metasurfaces[10]. The short skin depth and the inherent ohmic losses of metals, for instance, limit the achievable plasmonic sensing volume and LSPR-based detection of small molecules[11]. Similar bottlenecks are encountered for the harvesting of light in photo-catalysis, where injection of plasmon-generated hot electrons is insufficient to effectively drive important chemical pathways such as the oxygen evolution reaction[12]. Extending the use of the optical resonance of nanostructured metals in the visible regime to macro-scale volumes, while overcoming the opacity of bulk metals is focus of ongoing research efforts[13, 14].

Combining the attractive features of nanosized metals and semiconductors in multi-scale architectures with defined long- and short-term periodicities is a promising route for the design of three-dimensional photonic media. While being limited by lower near-field enhancement and weaker intrinsic properties than metallic nanomaterials[15], high-index semiconductors provide means to couple light into the nanoscale[16]. Achieving a three-dimensional arrangement of metallic and semiconductor nanomaterials over multiple length scales, however, has been elusive, and often resulted in poor control of the resulting media optical properties[17].

Recent progresses in the manufacturing of hybrid metal media have been achieved via e-beam lithography[18, 19] and wet-phase routes[20]. Despite the superior control over few layers permitted by e-beam lithography, extending its benefits to out of line-of-sight and multi-layered architectures is challenging[18]. Sol-gel colloidal methods and controlled DNA-mediated self-assembly of gold nanoparticles into three-dimensional superlattices have shown promising steps toward the fabrication of organic-metallic optical media[20]. Despite these promising breakthroughs in fabrication of organic-metallic optical media[14, 21], these structures require relatively laborious synthesis methods, lack of long-term stability outside a physiological environment, and their thickness is limited to the sub-micrometer scale. Extending these achievements to a larger selection of feasible materials and geometries bears much potential. The development of lithography-free techniques for manufacturing of three-dimensional metal-semiconductor media is subject of significant international efforts.

As an alternative route, the integration of metallic nanoparticles in a transparent fractal matrix is an unexplored route for the design of metal-semiconductor media with scale-invariant structural

features over large volumes. Indeed, aggregates of metallic nanoparticles exhibiting fractal properties are amongst the most efficient scattering enhancers[22] and have shown promising results in several research areas including giant local optical field[23], multi-functionality[24] and stabilised broadband optical chirality[25]. Depending on the nature of their recursive features, fractals can be roughly classified into two main categories: deterministic (mathematical) and stochastic (random) fractals[26]. The former class includes all the geometric fractals (such as the Mandelbrot set or the Sierpinski carpet), whose patterns rely on precise recursive mathematical formulations and can be more easily identified by their visual appearance. Oppositely, random fractals are patterns that, on their ensemble, have the remarkable property of having statistical self-similarity properties. Those patterns are very common in nature, as many natural laws follow a fractal scaling rule[27]. An archetype example of the stochastic category of fractals is provided by the diffusion-limited aggregation (DLA) processes[26], which includes physical phenomenon like dielectric breakdown, chemical dissolution, electrodeposition, dendritic solidification and some crystallization processes.

In our work, we fabricated self-similar networks of nanoparticles by self-assembly of hot aerosols. The resulting structures have previously determined as belonging to the random/stochastic fractal structures[28, 29]. In addition, nanoparticle fractals can be prepared by the aerosol self-assembly in the cluster-cluster agglomeration regime, providing a scalable mechanism for the fabrication of morphologies of semiconductors with sub-millimeter thickness[30].

Here, we introduce a methodology for the design and fabrication of inorganic photonic metamaterials with three-dimensionally controlled composition and periodicity over multiple length-scales. Our media architecture consists of resonant metallic nanoparticles dispersed with long-range uniformity, in transparent scaffolds of semiconductor nanoparticle fractals. This hybrid photonic media combines the advantages of a low-scattering, scale-invariant fractal scaffold with self-similar properties and periodic arrangement of resonant metal crystals. Titanium oxide nanoparticles were chosen as support of the plasmonic clusters in light of two key benefits of TiO_2: (i) high transparency at the plasmonic resonance frequency of the Au clusters; and (ii) a high surface energy that favours the adsorption of the VOC molecules, effectively increasing their local concentration in proximity of the Au nanoresonators.

Additionally, the ultra-porous nature of the TiO_2 fractal matrix facilitates the rapid diffusion and penetration of gaseous analytes throughout the whole layer, which is essential for efficient chemical sensing. Simulations of the propagation of electromagnetic waves through these fractal media reveal a net plasmonic near-field enhancement increase with media thickness increasing up to the microscale. It is important to note that this is the first report on an aerosol-made pure inorganic three-dimensional active media of plasmonic scatters. Most of current LSPR studies reported in the literature adopt a planar distribution of plasmonic particles, which imposes some limitations in terms of material layout and composition. Amongst other benefit, our approach enables to distribute plasmonic scatterers in three dimensions, achieving sub-100 nm separation of the Au particles and hence formation of three dimensional hot-spots with strong field localization. It also enables to extend the LSPR subwavelength phenomenon to the micron scale, still maintaining the advantageous evanescent and strongly localized features of the LSPR. As a representative first application, we demonstrate the use of this large plasmonic interaction volume to significantly enhance the sensitivity of localized surface plasmon resonance sensors with respect

to a bilayer system comprising of the same nanostructured materials. Our optimal metal-semiconductor architectures promptly reacts to volatile organic compounds at room temperature achieving detection limits of 0.01 vol%. We believe that these findings provide a general framework for the design of a new class of photonic metamaterials based on metal-semiconductor fractal media with applications ranging from light harvesting, photocatalysis, transformation optics and slow-light.

Results and Discussion

Figure 1a shows a schematic rendering of our photonic fractal media architecture. The latter consists of stochastically ordered gold nanocrystals, with uniform long-range periodicity, in a porous and transparent fractal scaffold of semiconductor nanoparticles. Fabrication of this three-dimensional architecture was conducted within a few seconds by on-the-flight mixing of twin nanoparticle aerosols, generated with a two nozzle flame reactor (see Supplementary Materials and Figure S1). The self-organization of the plasmonic and semiconductor nanoparticles via cluster-cluster agglomeration in the aerosol leads to a fractal material with self-repeating structural features from the nano- to the macro-scale[31]. Arbitrarily thick media arFige obtained by controlling the aerosol self-assembly time over a transparent substrate, with constant film growth rates in the range 32 nm s^{-1} (see Figure. S2).

Figure 1b shows a representative image of a fractal media, composed of gold and titanium oxide nanoparticles, with a thickness of 4.4 μm and a base of 75 mm by 25 mm. This Au-TiO_2 media was fabricated in a single step by exposure of the aerosol to a glass slide, used as a substrate, for 135 s. The presence of a uniform distribution of plasmonic gold nanoparticles is suggested by the uniform pink coloration of the media. A long range uniformity is also confirmed by the homogeneity of the media UV-Vis spectra, in various locations over its surface (see Figure S3). This is an advantageous feature, providing distinct benefits for the realization of commercial optical sensors[32].

An average media porosity of 95% was estimated from the optical and morphological measurements (see Supplementary Materials). This media porosity is below previous theoretical and experimental studies on diffusion-limited aerosol self-assembly of nanoparticle films[33]. The denser media morphology, observed here, is attributed to an enhanced particle sintering during deposition on the substrate, due to the higher surface substrate temperature generated by the twin aerosols. According to the Maxwell-Garnett effective medium theory, a media composition of 5% TiO_2 and 95% air voids is expected to decrease the effective refractive index (n_{eff}) at a wavelength of 560 nm from the TiO_2 bulk value of 2.6 to 1.1. This almost-unitary refractive index provides a quasi-transparent medium for the distribution of resonant plasmonic nanocrystals in a three-dimensional space.

The inner structure and composition of the media was investigated through a series of bulk and microscopic characterizations. X-ray diffraction indicates the exclusive presence of gold and TiO_2 with a cubic and anatase crystalline phase, respectively (Figure S4**)**. The average Au and TiO_2 crystal sizes can be tuned via the aerosol conditions, and were optimized to 19.4 ± 2 nm and 11.7 ± 1 nm, respectively, for subsequent application in optical sensing (see Figure S9). Notably,

varying the media thickness did not affect the average Au and TiO_2 crystal sizes, affording the individual tuning of near- and far-field features.

High resolution transmission electron microscopy provides further insights on the nanoscale arrangement of the Au and TiO_2 crystals (Figure 1c-d and Figure S5). Finely dispersed Au nanocrystals on an interconnected fractal backbone of TiO_2 nanoparticles were observed with high uniformity over areas of several square centimeters. Both the TiO_2 and Au nanoparticles have a spherical morphology with an average visible diameter of 13.5 nm and 11.2, respectively. At higher magnification, the (111) crystallographic plane lattice fringes of the Au *ffc* unit cell are visible (Figure 1d, inset). Their *d*-spacing of 0.24 nm further confirms the location of the Au nanocrystals[34] in the fractal structure.

The size and spatial density of the plasmonic nanocrystals can be tuned, adjusting the aerosols synthesis conditions (Figures S5 - S6**)**. For instance, increasing the Au aerosol mass concentration or its flow rate with respect to that of the TiO_2 aerosol increases the Au spatial density in the media from ca 320 NPs/μm^3 to 700 NPs/μm^3. Tuning of the media properties such as porosity can be achieved by controlling the extent of sintering during deposition, while preserving a fractal material. Small-angle X-ray spectroscopy (SAXS) measurements were performed to confirm the fractality of our architectures (Figure 1e). Indeed, SAXS experiments allow the direct measurement of the mass-fractal dimension of aggregates, which, corresponds to the slope of the spectra between the Guiner (low-q) and the Porod (high-q) regions[28, 35]. SAXS analysis shows that decreasing the media porosity from 95% to 93% results in relatively close fractal dimensions (D_f) of 1.85 and 1.83, respectively, in line with other reports that were measuring D_f of semiconductor oxides in the diffusion limited aggregation regime[24, 28]. These fractal dimensions were additionally confirmed by analysis of SEM images with a box-counting algorithm (see Supplementary Materials and Figure S7). The distinct morphological arrangement of these fractals is, however, indicated by their different lacunarity[36], which represents the texture heterogeneity of a fractal. We observed that the lacunarity increases, shifting toward longer length-scales, as the media porosity decreases. This is in line with the sintering of the TiO_2 nanoparticles, and formation of larger self-repeating units.

The three-dimensional arrangement of the plasmonic and semiconductor components within the media was mapped by scanning electron microscope (SEM) analysis (Figure 1f-g and Figure S2). The media consist of Au-TiO_2 fractals self-organized in a porous scaffold with a hierarchical distribution of meso- and macro-pores. Compositional contrasted images of the media were obtained using an angle-sensitive backscattered detector. The Au atoms are identified by the stronger deflection of incident electrons by heavier elements (Figures 1f and 1g). Bright back-scattering Au nanocrystals are observed with a uniform spatial distribution throughout the media cross-section and top surface. Analysis the Au nanocrystal particle size distribution in the horizontal and vertical planes reveal two quasi-identical lognormal distributions with a geometric mean and a geometric standard deviation (GSD) converging toward 14 - 15 nm and 1.5, respectively (Figure S5). This GSD is fairly close to the self-preserving value for Brownian's coagulation, indicating coalescence in the aerosol as the main growth mechanism of the Au nanocrystals.

The feasible media compositions are not limited to Au and TiO_2 matrixes and can be extended to a variety of semiconductors and dielectric metal oxides, as well as other metals. We have synthesized a set of resonant media with Au nanocrystals distributed in CuO, Fe_2O_3, and WO_3 fractal scaffolds (Figure S9). This provides a flexible route for the engineering of a large family of three-dimensional media of inorganic materials, with applications ranging from optical sensing and photocatalysis to optoelectronic and renewable energy harvesting.

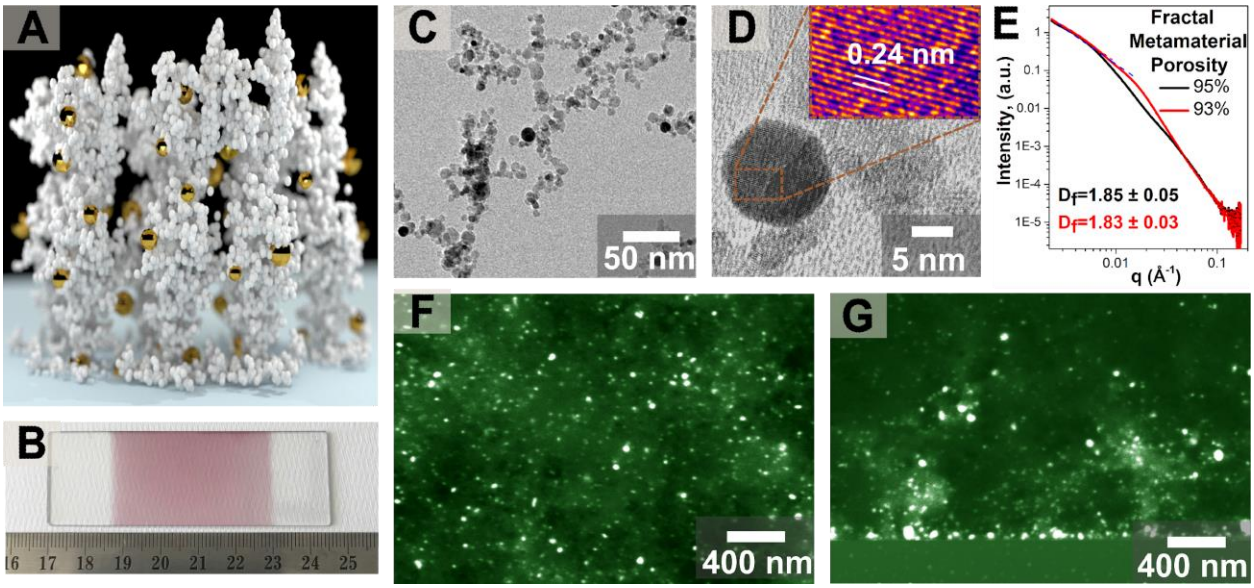

Figure. 1. Schematic and characterization. (a) schematic rendering of a resonant Au-TiO_2 media as a representative photonic fractal metamaterial. **(b)** Optical image of an Au-TiO_2 media on a glass slide. **(c-d)** Transmission electron micrograph of the collected nanoparticles and **d,** magnification of a single Au nanocrystal with the corresponding lattice d-spacing (inset). **(e)** Small angle X-ray scattering curve from fractal Au-TiO_2 media having different porosities of 95% and 93%, black and red lines, respectively, and respective fractal dimension (D_f). (**f-g**) Top-view and cross-sectional SEM images of a fractal Au-TiO_2 media on a silicon wafer. These images are taken with an angle-sensitive backscatter detector to provide a higher contrast for higher atomic number elements.

The possibility to self-assemble metallic nanoparticles in the three-dimensional space opens up a wide range of opportunities to obtain "hot spots" regions where the electromagnetic field is greatly enhanced. To demonstrate this, we have performed a set of finite-difference time-domain (FDTD) simulations using a planar (2D) and a 3D model systems comprising of hexagonal closed packed gold spheres (Figure S11) with an inter-particle separation of 1 nm. The results of these simulations, not surprisingly, show the presence of a higher number of hot spots in the cases of 3D distributed metallic centers, which in turn provides higher potential energy in the same analyzed volume.

To gain insight into the electromagnetic behavior of our fractal media, we have performed a set of FDTD simulations at optical frequencies. The fractal media were modelled by a fractal scaffold of TiO_2 nanoparticles with the same porosity, fractal dimension and equivalent distribution of gold nanocrystals as those experimentally observed. As a comparative model, a metasurface consisting of a two dimensional layer of Au nanocrystals was also simulated (**Figure 2a**). Figure 2b show the electric field enhancement ($|\mathbf{E}/\mathbf{E_0}|^2$) for the metasurface, evaluated at its localized surface plasmon resonance (LSPR) wavelength. A dipolar enhancement of the electric field, mostly confined, within the first 30 nm from the two dimensional Au layer is observed (Figure 2c-d). This is

conformal to the evanescent nature of LSPR field, and the limited interaction volume provided by plasmonic metasurfaces. In the space above these first 30 nm, the electric field enhancement exponentially decreases with the increasing distance from the metallic scattering centers, in line with the predicted behavior of plasmonic nanoparticles[37].

Figures 2e-h shows the electrodynamic response of the three-dimensional fractal media. In contrast to the metasurface, here, a significant and uniform net near-field $|\mathbf{E}/\mathbf{E_0}|^2$ enhancement is measured throughout the media volume with a characteristic dipolar behavior localized around each metallic scattering center. The theoretical upper limit for the field enhancement of these metamaterials is given by the optical extinction thickness of the wave in the media. Furthermore, the stochastically ordered nature of the Au distribution in the fractal TiO_2 space may result in some Au nanocrystals having close proximity. This induces LSPR coupling via near-field interaction, enabling additional high order resonance modes [38].

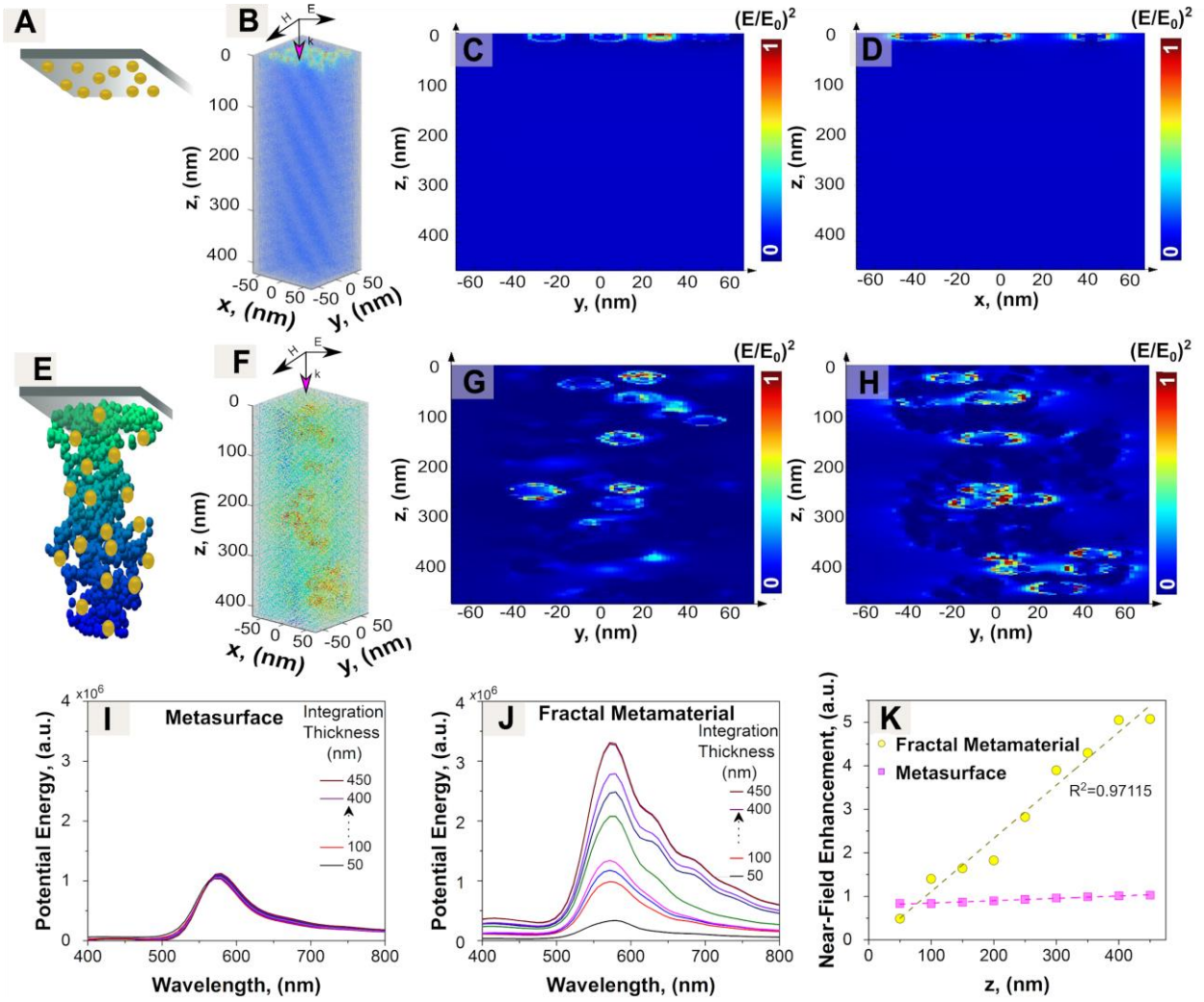

Figure. 2. Electrodynamic simulations. (**a**) Schematic of a comparative Au metasurface, consisting of a stochastic planar distribution of Au nanoparticles onto a quartz substrate. (**b**) volumetric $|\mathbf{E}/\mathbf{E_0}|^2$ field distribution on-resonance obtained by FDTD simulations. (**c-d)** Cross-section slices at different positions of the $|\mathbf{E}/\mathbf{E_0}|^2$ enhancement for the Au metasurface structure. **(e)** Schematic of the fractal Au-TiO_2 metamaterial, consisting of Au crystals stochastically distributed in a three-dimensional TiO_2 fractal scaffold. (**f**) volumetric distribution of the $|\mathbf{E}/\mathbf{E_0}|^2$ field at LSPR resonance. (**g-h**) Cross-section slices at different positions of the $|\mathbf{E}/\mathbf{E_0}|^2$ enhancement for the 3D Au-TiO_2 structure.

(**i-j**) Cumulative distribution of field enhancement $|\mathbf{E}/\mathbf{E_0}|^2$: integration over an increasing volume (sampled every 50 nm) as a function of the wavelength for the metasurface and the 3D structure, respectively. (**k)** Near-field enhancement (integral of the potential energy over the wavelengths) for the studied structures.

The quantitative field enhancement in the metamaterial and metasurface were computed by the cumulative volume integration of the $|\mathbf{E}/\mathbf{E_0}|^2$ in the media (See Supplementary Information). For the metasurface, the integration over the volume provides maximum potential energy in the band of 500-650 nm (Figure 2i), arising from strong interacting plasmonic modes. The evanescent nature of the plasmonic resonance confines the near-field within the first 30-50 nm from the Au layer. The additional media volume above this first 50 nm has a negligible contribution to the total potential energy (Figure 2i). In contrast, in the fractal metamaterial, a constantly increasing potential energy is measured with increasing media volume (Figure 2j). Some small shoulders are observed in the 600-700 nm wavelength regions and attributed to higher resonant modes arising from the LSPR coupling between closely spaced Au particles in the fractal TiO_2 scaffold. Overall, in the metamaterial, the three-dimensional distribution of the Au nanocrystals enhances the peak potential energy of the media by more than 190% with respect to the metasurface.

Further integration over the wavelengths provides the overall plasmonic enhancement due to the volumetric distribution of the Au nanoparticles. Figure 2k shows the cumulative near-field enhancement integrated over the entire visible range as a function of the media thickness (see Supplementary Information). For the metasurface, above 50 nm from the Au layer, the near-field enhancement with increasing media thickness is quasi negligible. In contrast, in the metamaterial the field enhancement increases linearly (goodness of fit R^2=0.97115) with increasing film thickness. An enhancement of 278% over that of the metasurface is computed for a metamaterial thickness of 450 nm. It should be noted that while the simulations were limited to a thickness of 450 nm, the metamaterials fabricated here, have a thickness of up to ~17 μm (see Figure S2). The latter are expected to lead to higher field enhancements. Further discussion of the FDTD analysis is provided in the Supplementary Methods. These simulations indicate that the evanescent nanoscale plasmonic field enhancement effect can be extended into the micro-scale, while maintaining the advantageous subwavelength and strongly localized features of LSPR.

The far-field optical properties of these fractal metamaterials were investigated by UV-Vis angular resolved specular transmittance and reflectance spectroscopy (Figure 3a-e). Increasing the thickness of the fractal media from *ca* 1.5 to 6.1 μm shifts their wavelength-dependent extinction spectra (ε) from a transparent (< 30% ε_{max}) to an opaque state (> 80% ε_{max}), while preserving the plasmonic resonance frequency in the range of 500-600 nm. The plasmonic region of the extinction spectra shows a continuous increase with a quasi-negligible broadening up to a media's thickness of 4.4 μm. At a media thickness of 6.1 μm, a broadening and red-shift of the plasmonic extinction region are observed. Further UV-Vis analysis is provided in Figure S10. Recent studies have indicated a correlation between agglomerate size and shape and far-field optical properties[39, 40]. It has been proposed that weakly coupled plasmonic superlattices optically behave similarly to a single metallic nanoparticle, allowing studying the systems in terms of effective bulk properties[39, 41]. As such, here, the spectral broadening in the plasmonic extinction region of the media at a thickness above 4.4 μm is attributed to the predominance of photonic modes arising from the micro-scale size of the fractal scaffold. Furthermore, since the bandgap of TiO_2 falls in the UV region, the latter results highly transparent in the visible and doesn't majorly influence the spectral position of the LSPR.

The optical behavior of these fractal metamaterials was further investigated by polarization dependent angular resolved specular transmittance and reflectance spectroscopy. A 4.4 μm thick fractal metamaterial and a comparative metasurface with a two-dimensional distribution of the Au nanocrystals are shown as representative materials (Figure 3b-e and Figure S16). In the fractal metamaterial, the resonant plasmonic band is angle-independent while in the metasurface a slight LSPR shift is observed with increasing incident angle. Furthermore, whereas the latter metasurface possess transmittance intensities always below 15% at the λ_{LSPR}, the fractal metamaterial transmittance is strongly dependent from the incident angle. At high incidents angles, the light transmittance at the plasmonic resonance frequency is *ca* 10% and progressively increases with decreasing incident angle, reaching 50% for an orthogonal irradiation angle to the substrate surface. This is attributed to the spatial distributions of the resonant Au nanocrystals in the metasurface and in our fractal metamaterial. While in the metasurface the plasmonic material is confined within a thin layer of few hundred nanometers from the substrate surface, in fractal metamaterial the Au is distributed throughout thousands of nanometers above the substrate. As a result, for the metamaterial increasing the light incident angle significantly increases the optical path length, while it has a quasi-negligible impact for the metasurface.

As a representative application, we demonstrate the use of these fractal metamaterials as optical sensors for volatile molecules. Localized surface plasmon resonance has been broadly used for bio- and chemical-sensing in liquid environments as they provide sufficiently high refractive index contrast in the range of 10^{-2} [42]. Application of plasmonic sensing to the measurement of molecules in gases has been proven very challenging, as the induced variation in refractive index at room temperature is usually less than 10^{-4}. A range of nanoscale architectures relying on optimized planar structures, nano-antennas and integration of other sensing materials (porous matrix, metal-organic frameworks, two-dimensional materials) have been proposed to overcome this challenge[9, 32, 43]. Additionally, parts per million (ppm) detection of gaseous analytes has been achieved by increasing the operative temperature of the systems to favor the charge transfer between plasmonic elements and gases[44] or by employing similar optical platforms with resonances in the near-infrared region of the electromagnetic spectrum[45]. Table 1 shows an exemplary collection of these works.

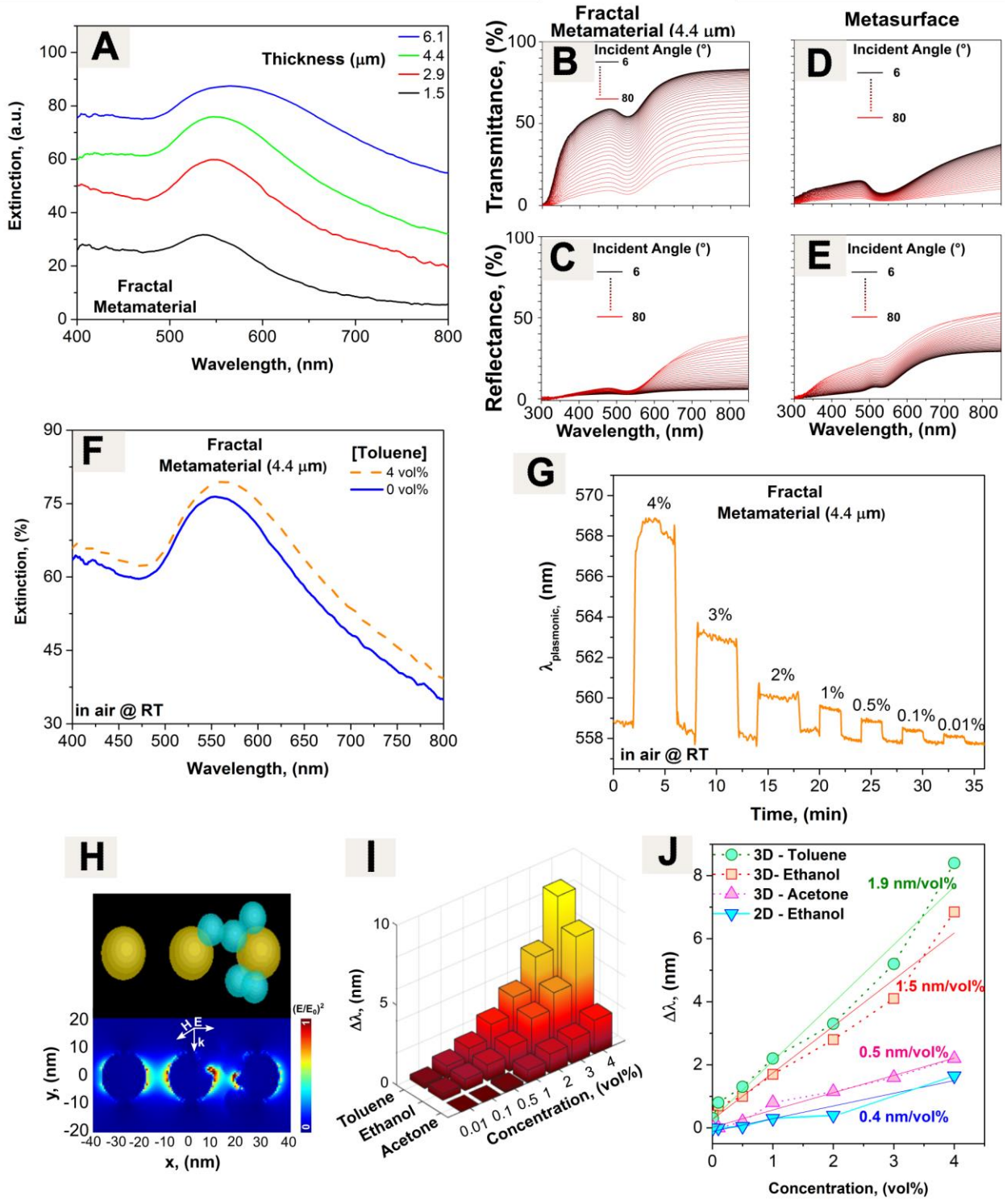

Figure 3. Optical properties and sensing. (**a)** UV-Vis extinction of fractal metamaterials as a function of their thickness. **(b-e)** Angular dependent transmittance and specular reflectance of the 4.4 μm fractal Au-TiO_2 media and a metasurface consisting of stochastically distributed Au nanocrystals. **(f)** UV-Vis spectrum of the 4.4 μm fractal metamaterial in air and under the exposure of 4 vol% of toluene gas molecules at room temperature. **(g)** Dynamic response the LSPR centroid of the same sample when exposed to different concentration of toluene. (**h**) Schematic (top) and computed electric field enhancement at resonance (bottom) of a model system comprising of equidistant Au spheres in air. To be noted that the amplification is greater in presence of the TiO_2 nanoparticles, where the most of

the condensation occurs. (**i**) Summary of the plasmonic shift of the 4.4 μm fractal metamaterial to different gaseous analytes and concentration. (**j**) Comparison between the limit of detection of the fractal metamaterial and the Au metasurface, as a function of analyte concentration.

Here, we demonstrate the use of the large plasmonic sensing volume of these fractal metamaterials to achieve room-temperature detection of gas molecules with a limit of detection of 0.01 vol%. Figure 3f shows the extinction spectrum of a 4.4 μm-thick fractal media in pure air and with 4 vol% toluene at room temperature. The introduction of the toluene gas molecules results in a visible shift of the extinction spectrum through the media, corresponding to a red-shift of the plasmonic resonance wavelength of 8.4 nm. This huge shift due to gas phase analytes is in a comparable range to that observed for sensing of biomolecules in liquid environments[46].

Figure 3g shows real-time tracking of the plasmonic resonance shift during on/off injection of various concentrations of toluene in the air at room temperature. A rapid room-temperature response dynamics to the toluene gas molecule presence is observed down to 0.01 vol%. Both response and recovery times are in the order of 5 s, and thus very fast for room-temperature plasmonic sensing.

Table 1. LSPR gas and chemical sensing platforms with operative parameters and limits of detection.

Materials	**Operative Temperature and Wavelength**	**Analyte**	**LSPR shift**	**Limit of Detection**	**Sensitivity (nm/vol%) ***	**Ref**
Au-TiO_2 fractals	RT, $\lambda_{LSPR}\approx$550 nm	Different VOCs	0.3 nm @ 0.01 vol%	<0.01 vol%	0.5 – 1.9 nm/vol%	This work
Ag NPs	RT $\lambda_{LSPR}\approx$702 nm	Ar/ He in N_2	~0.058 nm for 100 vol% He/N_2 switch	NA	0.00058 nm/vol%	[47]
Modified Ag NPs	RT, $\lambda_{LSPR}\approx$400 nm	Different VOCs	~0.3 nm @ 0.066 vol% of m-xylene	0.02-0.05 vol%	1.24 nm/vol%	[48]
Ag-MOF (HKUST-1)	RT, $\lambda_{LSPR}\approx$661 nm	CO_2 and SF_6	1.88 nm at 100 vol% of CO_2	33 vol%	0.03 nm/vol%* Computed in the linear region	[49]
Au-YSZ film	500 °C, $\lambda_{LSPR}\approx$600 nm	NO_2	~0.07 nm @ 0.0005 vol%	0.0005 vol%	18-130 nm/vol%	[50]
Au-CeO_2	300 °C, $\lambda_{LSPR}\approx$675 nm	H_2	15 nm @ 20 vol%	0.38 vol%	-0.31 nm/vol%	[51]
Layered Au-MgF_2-Pd wires	RT, $\lambda_{LSPR}\approx$650 nm	H_2	19 nm @ 4 vol%	0.5 vol%	4.2 nm/vol%	[52]
Au-dot and porous SiO_2	RT, $\lambda_{LSPR}\approx$1250 nm	Different VOCs	~20 nm @ 2.6 vol%	Extrapolated 0.0004 vol%	4.5 nm/vol%	[53]

Indium nanograins	RT, λLSPR≈300 nm	Ethanol and acetone	~2 nm @ 0.05 vol%	0.05 vol%	0.3 nm/vol% @ high concentration 20 nm/vol% low concentration	[54]
Functionalized Au NPs	RT, λLSPR≈300 nm	Glycerin	~6 nm @ 10 vol%	12.46 nM	0.845 nm/vol%	[55]

*The sensitivity expressed in nm/vol% were computed from the experimental results of the respective research works.

A fundamental advantage of our fractal metamaterial is caused by the ultra-porous nature of the semiconductor matrix. This platform indeed offers multifold reasons to enhance the performance of these LSPR sensors. Such a substantial increased surface area given by the porous texture of the metamaterial facilitate the gas penetration and adsorption throughout the scaffold, thus ensuring quick and reversible response and recovery times. Moreover, it significantly increases the amount of analyte that can be incorporated into the matrix, maximizing the `biological' sensitivity of the system[11, 56]. Importantly, the micro- and meso- porosity and the large surface-to-volume ratio of our fractal media favors the accumulation of the VOCs on the surface resulting in a capillary condensation, which in turn leads to an increased local refractive index[53, 57]. Furthermore, the stochastic nature of the aerosol self-assembly process leads to a distribution of Au nanoparticles with interparticle distances in the order of ~20-100 nm (Figure 1c and Figure S5). The close proximity of metal nanoparticles results in a three dimensional distribution of hot-spots where the electric field is significantly enhanced[58] (see Figure S11), which is ideal for sensing applications. This field enhancement further increases the amplification of the plasmonic response toward the VOCs analytes. Additionally, as represented in Figure 3h, the larger refractive index of TiO_2, with respect to the background, acts as an electric field sink and pulls the plasmonic field toward the high surface-energy semiconductor, where the most of condensation happens, contributing in enhancing the gas sensing performance.

The condensation mechanism is further confirmed by performing sensing experiments with CO_2, an inert and non-condensing gas at room temperature and standard pressure (See Figure S13). Despite the higher concentration of CO_2 used (10 vol %), there is no significant red-shift of the LSPR wavelength, which endorses the formation of a thin condensate layer in the presence of VOCs that leads to an increased local refractive index which, in turn, contributes to improve the sensitivity and lower the limit of detection. Furthermore, electron transfer from the VOCs to semiconductor surfaces such as TiO_2 and ZnO has been broadly reported for chemo-resistive gas sensing and UV photodetectors[59]. Here, electron exchange from the VOCs to the accessible TiO_2 surface may further contribute to the enhancement of the plasmonic response[60].

Our fractal metamaterials were tested against various other VOCs, including ethanol and acetone. Exposure to volatile compounds always led to a red-shift of the plasmonic resonance wavelength, in line with the induced increase in the local refractive index. The magnitude of the red-shift was dependent from the gas molecule and their concentration (Figure 3i), showing a stronger response for less volatile compounds. Coherently with the condensation mechanism, acetone –which has the lowest evaporation temperature among the tested VOCs (T_{ev}=56 °C)– shows the lowest sensitivity and limit of detection of 0.5 vol%.

It is also important to note that while there is an initial monotonous increase in sensitivity with increasing fractal media thickness, this reaches a maximum for a fractal thickness of *ca* 4.4 µm and thereafter decreases again (Figure S12). This attributed to other factors such as the introduction of photonic modes arising from the micro-scale size of our fractal scaffold[39] that are indicated by the broadening of the plasmonic absorption spectrum (Figure 3a).

The performance of these metamaterials was benchmarked to that of an optimized metasurface with a two dimensional gold nanocrystal distributions with a layer of TiO_2 integrated (Figure S16). Figure 3j shows the shift in the plasmonic resonance wavelength as a function of different analytes concentrations, for the metamaterials and the metasurface. Notably, while the metasurface has a limit of detection of 1 vol% with a shift of the λ_{LSPR} = 0.3 nm, the metamaterial has the capability to lower the detection limit by two orders of magnitude, producing a shift of 0.3 nm with 0.01 vol% for toluene at room temperature (see Figure S13).

Here, we have computed the sensitivity in terms LSPR wavelength shift (nm) per volume percentage of the gaseous analytes ($S = \Delta\lambda/vol\%$). This definition is useful to describe the sensitivity of systems where an accumulation of the gaseous analyte occurs. This definition no longer requires an estimation of the environmental refractive indices. Thus one can evaluate the system sensitivity in terms of the actual volume of gaseous analytes injected in the sensing chamber. Figure 3j shows the results of this analysis for a 4.4 µm thick Au-TiO_2 fractal media. Not surprisingly, the planar metasurface has the lowest sensitivity (~0.4 nm/vol%), followed by the 3D architecture against acetone (~0.54 nm/vol%) which is the VOC that condensate the least at room temperature. Interesting, an enhancement in sensitivity by a factor of ca. ~3-5, with respect to the planar structure, is shown by the 3D metamaterial for ethanol and toluene. Furthermore, as shown in Table 1, our results are on the higher side of the sensitivity spectrum, with respect to, other LSPR gas sensing platforms: an important advantage that, when normalized to the flexibility of our synthesis approach and the wide tuneability, could give access to a novel sensitive platform for biochemical sensing and photocatalysis.

However, despite the high sensitivity measured in the gas-phase, the fractal media are not yet suitable for measuring refractive index changes in a liquid environment. We have tested our metamaterial in two different liquid, namely water and ethanol (Figure S14). The change of environment is promptly reflected in a red-shift of the LSPR wavelength of about 20 nm when going from air to water, and an additional ~10 nm of shift is measured when the environment is changed to ethanol (n_{water}=1.33, $n_{ethanol}$=1.36). However, due to the low mechanical stability – intrinsically correlated to the high porosity– the fractal matrix collapses after the exposure to the liquids, resulting in a damped and broadened optical spectra. To improve the mechanical stability for plasmonic measurement of liquid environment, further optimization of the media porosity is required as previously reported[61].

Conclusion

We have developed a class of photonic fractal metamaterials consisting of resonant metallic nanoparticles stochastically ordered in three-dimensional fractal semiconductors having quasi-unitary effective refractive indexes. Exploiting the uniformity and long-range periodicity of the fractal space, we designed a range of resonant plasmonic media with accurately controlled thickness, density and loading of the nanoresonators. Our simulations indicate that the volumetric

distribution of the gold nanocrystals results in continuous enhancement of the plasmonic interaction volume throughout the media thickness, overcoming the optical limitations of two-dimensional metasurfaces. We demonstrate a potential use of these fractal metamaterials for optical sensing, achieving the fully optical detection of 0.01 vol% of gaseous analyte at room temperature, obtaining a limit of detection two orders of magnitude superior to that of high-performing gold metasurfaces. This new class of fractal metamaterials provide tunable and scalable optical features with fascinating potential for the development of high-end sensing, catalysis and optoelectronic applications.

Acknowledgments

The research leading to these results has received funding from the ANU Grand Challenge Scheme, Our Health in Our Hands. The authors also acknowledge the financial support by the Australian Research Council (ARC). A.T. gratefully acknowledges the support of the ARC DP150101939 and the ARC DE160100569. M.R. sincerely appreciates the supports from the Royal Society Wolfson Fellowship. All the authors acknowledge the use of the Australian National Fabrication Facility (ANFF), ACT Node, and the Centre of Advanced Microscopy (CAM) at ANU. Part of the research was undertaken at the SAXS/WAXS beamline at the Australian Synchrotron, part of ANSTO, and we thank the beamline scientists for their technical assistance.

References

[1] R. A. Shelby, D. R. Smith, S. Schultz, Science 2001, 292, 77; N. Fang, H. Lee, C. Sun, X. Zhang, Science 2005, 308, 534; D. Schurig, J. J. Mock, B. J. Justice, S. A. Cummer, J. B. Pendry, A. F. Starr, D. R. Smith, Science 2006, 314, 977; H. N. S. Krishnamoorthy, Z. Jacob, E. Narimanov, I. Kretzschmar, V. M. Menon, Science 2012, 336, 205; D. Ayuso, O. Neufeld, A. F. Ordonez, P. Decleva, G. Lerner, O. Cohen, M. Ivanov, O. Smirnova, Nature Photonics 2019; Z. Fusco, M. Taheri, R. Bo, T. Tran-Phu, H. Chen, X. Guo, Y. Zhu, T. Tsuzuki, T. P. White, A. Tricoli, Nano Letters 2020, 20, 3970.

[2] K. L. Kelly, E. Coronado, L. L. Zhao, G. C. Schatz, The Journal of Physical Chemistry B 2003, 107, 668.

[3] K. Kumar, H. Duan, R. S. Hegde, S. C. W. Koh, J. N. Wei, J. K. W. Yang, Nature Nanotechnology 2012, 7, 557.

[4] C. Fei Guo, T. Sun, F. Cao, Q. Liu, Z. Ren, Light: Science &Amp; Applications 2014, 3, e161.

[5] S. A. Maier, P. G. Kik, H. A. Atwater, S. Meltzer, E. Harel, B. E. Koel, A. A. G. Requicha, Nat Mater 2003, 2, 229.

[6] Z. Xuming, C. Yu Lim, L. Ru-Shi, T. Din Ping, Reports on Progress in Physics 2013, 76, 046401.

[7] M. S. Tame, K. R. McEnery, Ş. K. Özdemir, J. Lee, S. A. Maier, M. S. Kim, Nature Physics 2013, 9, 329.

[8] F. Yesilkoy, R. A. Terborg, J. Pello, A. A. Belushkin, Y. Jahani, V. Pruneri, H. Altug, Light: Science &Amp; Applications 2018, 7, 17152; Z. Fusco, R. Bo, Y. Wang, N. Motta, H. Chen, A. Tricoli, Journal of Materials Chemistry C 2019, 7, 6308.

[9] N. Liu, M. L. Tang, M. Hentschel, H. Giessen, A. P. Alivisatos, Nature Materials 2011, 10, 631.

[10] N. Liu, H. Guo, L. Fu, S. Kaiser, H. Schweizer, H. Giessen, Nature Materials 2008, 7, 31; C. M. Soukoulis, M. Wegener, Nature Photonics 2011, 5, 523.

[11] J. J. Mock, R. T. Hill, Y.-J. Tsai, A. Chilkoti, D. R. Smith, Nano Letters 2012, 12, 1757.

[12] Y. Dubi, Y. Sivan, Light: Science & Applications 2019, 8, 89.

[13] V. N. Rai, A. K. Srivastava, C. Mukherjee, S. K. Deb, Applied Optics 2012, 51, 2606; T. Tanaka, A. Ishikawa, Nano Converg 2017, 4, 34.

[14] A. S. Urban, X. Shen, Y. Wang, N. Large, H. Wang, M. W. Knight, P. Nordlander, H. Chen, N. J. Halas, Nano Lett 2013, 13, 4399.

[15] M. Caldarola, P. Albella, E. Cortés, M. Rahmani, T. Roschuk, G. Grinblat, R. F. Oulton, A. V. Bragas, S. A. Maier, Nature Communications 2015, 6, 7915.

[16] I. Staude, J. Schilling, Nature Photonics 2017, 11, 274; I. Staude, A. E. Miroshnichenko, M. Decker, N. T. Fofang, S. Liu, E. Gonzales, J. Dominguez, T. S. Luk, D. N. Neshev, I. Brener, a. Kivshar†, ACS Nano 2013, 7, 7824.

[17] A. Travesset, Science 2011, 334, 183; C. M. Soukoulis, M. Wegener, Nature Photonics 2011, 5, 523.

[18] N. Liu, H. Guo, L. Fu, S. Kaiser, H. Schweizer, H. Giessen, Nature Materials 2007, 7, 31; F. Miyamaru, S. Kuboda, K. Taima, K. Takano, M. Hangyo, M. W. Takeda, Applied Physics Letters 2010, 96, 081105; L. Na, F. Liwei, K. Stefan, S. Heinz, G. Harald, Advanced Materials 2008, 20, 3859.

[19] R. Mohsen, L. Giuseppe, B. Igal, V. Z. Anatoly, A. M. Stefan, A. Costantino De, T. Hoe, G. Valerio Flavio, K. Fouad, O. Rupert, V. Kaushal, L. Mykhaylo, S. Isabelle, X. Lei, E. M. Andrey, J. Chennupati, N. N. Dragomir, OEA 2018, 1, 180021.
[20] P. M. Tessier, O. D. Velev, A. T. Kalambur, J. F. Rabolt, A. M. Lenhoff, E. W. Kaler, Journal of the American Chemical Society 2000, 122, 9554; S. Y. Park, A. K. R. Lytton-Jean, B. Lee, S. Weigand, G. C. Schatz, C. A. Mirkin, Nature 2008, 451, 553; D. Nykypanchuk, M. M. Maye, D. van der Lelie, O. Gang, Nature 2008, 451, 549; S. J. Barrow, X. Wei, J. S. Baldauf, A. M. Funston, P. Mulvaney, Nature Communications 2012, 3, 1275; A. S. Urban, X. Shen, Y. Wang, N. Large, H. Wang, M. W. Knight, P. Nordlander, H. Chen, N. J. Halas, Nano Letters 2013, 13, 4399.
[21] S. Y. Park, A. K. Lytton-Jean, B. Lee, S. Weigand, G. C. Schatz, C. A. Mirkin, Nature 2008, 451, 553; D. Nykypanchuk, M. M. Maye, D. van der Lelie, O. Gang, Nature 2008, 451, 549.
[22] M. Stockman, Physics 2010, 3.
[23] K. Li, M. I. Stockman, D. J. Bergman, Phys Rev Lett 2003, 91, 227402.
[24] T. Tran-Phu, R. Daiyan, Z. Fusco, Z. Ma, L. R. A. Rahim, A. Kiy, P. Kluth, X. Guo, Y. Zhu, H. Chen, R. Amal, A. Tricoli, Journal of Materials Chemistry A 2020.
[25] M. L. Tseng, Z.-H. Lin, H. Y. Kuo, T.-T. Huang, Y.-T. Huang, T. L. Chung, C. H. Chu, J.-S. Huang, D. P. Tsai, Advanced Optical Materials 2019, 7, 1900617.
[26] H. E. Stanley, *Fractals and Disordered Systems*, Springer-Verlag Berlin Heidelberg, 1996.
[27] J. H. Brown, V. K. Gupta, B. L. Li, B. T. Milne, C. Restrepo, G. B. West, Philos Trans R Soc Lond B Biol Sci 2002, 357, 619.
[28] G. Beaucage, H. K. Kammler, R. Mueller, R. Strobel, N. Agashe, S. E. Pratsinis, T. Narayanan, Nature Materials 2004, 3, 370.
[29] B. Buesser, S. E. Pratsinis, Annu Rev Chem Biomol Eng 2012, 3, 103.
[30] A. Tricoli, S. E. Pratsinis, Nature Nanotechnology 2010, 5, 54.
[31] J. Hyeon-Lee, G. Beaucage, S. E. Pratsinis, S. Vemury, Langmuir 1998, 14, 5751; T. Tran-Phu, R. Daiyan, Z. Fusco, Z. Ma, R. Amal, A. Tricoli, Advanced Functional Materials 2020, 30, 1906478.
[32] Z. Fusco, M. Rahmani, R. Bo, T. Tran-Phu, M. Lockrey, N. Motta, D. Neshev, A. Tricoli, Advanced Functional Materials 2019, 29, 1806387.
[33] A. Tricoli, G. Markus, F. Mayer, S. Kuühne, A. Hierlemann, P. S. E., Advanced Materials 2008, 20, 3005; S. M. J. L. Castillo, D. Rodriguez-Perez, A. Perea, P. L. Garcia-Ybarra, KONA Powder and Particle Journal 2014, 31, 214.
[34] J. Wu, X. Zan, S. Li, Y. Liu, C. Cui, B. Zou, W. Zhang, H. Xu, H. Duan, D. Tian, W. Huang, F. Huo, Nanoscale 2014, 6, 749.
[35] P. S. Bauer, H. Amenitsch, B. Baumgartner, G. Köberl, C. Rentenberger, P. M. Winkler, Nature Communications 2019, 10, 1122.
[36] Z. Fusco, M. Rahmani, R. Bo, R. Verre, N. Motta, M. Käll, D. Neshev, A. Tricoli, Advanced Materials 2018, 30, 1800931.
[37] A. J. Haes, S. Zou, G. C. Schatz, R. P. Van Duyne, The Journal of Physical Chemistry B 2004, 108, 6961.
[38] N. Jiang, X. Zhuo, J. Wang, Chemical Reviews 2018, 118, 3054.
[39] M. B. Ross, C. A. Mirkin, G. C. Schatz, The Journal of Physical Chemistry C 2016, 120, 816.

[40] S. Y. Park, J.-S. Lee, D. Georganopoulou, C. A. Mirkin, G. C. Schatz, The Journal of Physical Chemistry B 2006, 110, 12673; J. J. Storhoff, A. A. Lazarides, R. C. Mucic, C. A. Mirkin, R. L. Letsinger, G. C. Schatz, Journal of the American Chemical Society 2000, 122, 4640.
[41] K. L. Young, R. M. B., M. G. Blaber, M. Rycenga, M. R. Jones, C. Zhang, A. J. Senesi, B. Lee, G. C. Schatz, C. A. Mirkin, Advanced Materials 2014, 26, 653; M. B. Ross, J. C. Ku, V. M. Vaccarezza, G. C. Schatz, C. A. Mirkin, Nature Nanotechnology 2015, 10, 453; M. B. Ross, M. G. Blaber, G. C. Schatz, Nature Communications 2014, 5, 4090.
[42] J. N. Anker, W. P. Hall, O. Lyandres, N. C. Shah, J. Zhao, R. P. Van Duyne, Nature Materials 2008, 7, 442.
[43] J. M. Bingham, J. N. Anker, L. E. Kreno, R. P. V. Duyne, Journal of the American Chemical Society 2010, 132; L. E. Kreno, J. T. Hupp, R. P. V. Duyne, Anal Chem 2010, 82, 8040.
[44] M. Ando, T. Kobayashi, S. Iijima, M. Haruta, Sensors and Actuators B: Chemical 2003, 96, 589; P. H. Rogers, G. Sirinakis, M. A. Carpenter, The Journal of Physical Chemistry C 2008, 112, 6749.
[45] Y. Wu, B. Yao, A. Zhang, Y. Rao, Z. Wang, Y. Cheng, Y. Gong, W. Zhang, Y. Chen, K. S. Chiang, Opt. Lett. 2014, 39, 1235; B. Yao, C. Yu, Y. Wu, S.-W. Huang, H. Wu, Y. Gong, Y. Chen, Y. Li, C. W. Wong, X. Fan, Y. Rao, Nano Letters 2017, 17, 4996; Nebiyu A. Yebo, Petra Lommens, Zeger Hens, R. Baets, Optics Express 2010, 18.
[46] A. E. Cetin, D. Etezadi, B. C. Galarreta, M. P. Busson, Y. Eksioglu, H. Altug, ACS Photonics 2015, 2, 1167.
[47] J. M. Bingham, J. N. Anker, L. E. Kreno, R. P. Van Duyne, Journal of the American Chemical Society 2010, 132, 17358.
[48] Y.-Q. Chen, C.-J. Lu, Sensors and Actuators B: Chemical 2009, 135, 492.
[49] L. E. Kreno, J. T. Hupp, R. P. Van Duyne, Analytical Chemistry 2010, 82, 8042.
[50] P. H. Rogers, G. Sirinakis, M. A. Carpenter, The Journal of Physical Chemistry C 2008, 112, 8784.
[51] N. M. Houlihan, N. Karker, R. A. Potyrailo, M. A. Carpenter, ACS Sensors 2018, 3, 2684.
[52] A. Tittl, P. Mai, R. Taubert, D. Dregely, N. Liu, H. Giessen, Nano Letters 2011, 11, 4366.
[53] A. Monkawa, T. Nakagawa, H. Sugimori, E. Kazawa, K. Sibamoto, T. Takei, M. Haruta, Sensors and Actuators B: Chemical 2014, 196, 1.
[54] M. Honda, Y. Ichikawa, A. G. Rozhin, S. A. Kulinich, Applied Physics Express 2017, 11, 012001.
[55] J.-G. Walter, A. Eilers, L. S. M. Alwis, B. W. Roth, K. Bremer, Sensors 2020, 20, 2889.
[56] A. V. Kabashin, P. Evans, S. Pastkovsky, W. Hendren, G. A. Wurtz, R. Atkinson, R. Pollard, V. A. Podolskiy, A. V. Zayats, Nature Materials 2009, 8, 867.
[57] Y. Takimoto, A. Monkawa, K. Nagata, M. Kobayashi, M. Kinoshita, T. Gessei, T. Mori, H. Kagi, Plasmonics 2020, 15, 805.
[58] E. Petryayeva, U. J. Krull, Analytica Chimica Acta 2011, 706, 8.
[59] N. Nasiri, R. Bo, T. F. Hung, V. A. L. Roy, L. Fu, A. Tricoli, Advanced Functional Materials 2016, 26, 7359.
[60] A. Barchanski, *Laser-Generated Functional Nanoparticle Bioconjugates: Design for Application in Biomedical Science and Reproductive Biology*, Springer Spektrum, 2016.

[61] A. Tricoli, A. S. Wallerand, M. Righettoni, Journal of Materials Chemistry 2012, 22, 14254; A. Tricoli, N. Nasiri, H. Chen, A. S. Wallerand, M. Righettoni, Solar Energy 2016, 136, 553.